Microstructure as a key parameter for understanding chloride ingress in alkali-activated mortars

Runci, Antonino; Provis, John; Serdar, Marijana

DIGITALNI AKADEMSKI ARHIVI I REPOZITORIJI

Microstructure as a key parameter for understanding chloride ingress in alkali-activated mortars

3 authors:

Antonino Runci
Flemish Institute for Technological Research
8 PUBLICATIONS   72 CITATIONS

SEE PROFILE

John Provis
Paul Scherrer Institut
500 PUBLICATIONS   52,176 CITATIONS

SEE PROFILE

Marijana Serdar
University of Zagreb
131 PUBLICATIONS   1,415 CITATIONS

SEE PROFILE

Microstructure as a key parameter for understanding chloride ingress in alkali-activated mortars

Antonino Runci [a], John Provis [b], Marijana Serdar [a,*]

[a] *University of Zagreb, Faculty of Civil Engineering, Department of Materials, Croatia*
[b] *University of Sheffield, Department of Materials Science and Engineering, UK*

A B S T R A C T

This study aims to evaluate the influence of microstructural properties on the chloride diffusion resistance of alkali-activated materials (AAMs) based on blast furnace slag and/or fly ash, with variable activator doses (represented as $Na_2O\%$). Resistance to chloride penetration was tested using accelerated chloride penetration (NT BUILD 443) and chloride migration (NT BUILD 492) tests. Addition of slag to alkali-activated mortars mainly based on fly ash reduced porosity and chloride permeability. Chloride penetration decreased with increasing $Na_2O\%$, but porosity and pore structure did not follow the same trend. The pore threshold (d_{th}) and critical pore radius (r_{crit}) determined by mercury intrusion porosimetry had a good correlation with the chloride diffusion coefficient. Both the quantification of reaction products and the correlation between chloride penetration and pore surface area indicated that physical chloride adsorption on the C-A-S-H/N-A-S-H gel surfaces predominated over chemical chloride binding.

1. Introduction

Chloride ingress into reinforced concrete is a key parameter that determines the service life of concrete structures. In marine environments and/or when de-icing salts are used, chloride anions can penetrate by capillary absorption, hydrostatic pressure, migration, and/or diffusion. Chloride anions generally have little effect on concrete stability in terms of their interactions with hydrate products. However, when the anions penetrate to the embedded reinforcement, their accumulation can lead to steel corrosion. As a consequence of this corrosion, the pitting and loss of cross-section leads to weakening of the reinforcement, formation of expansive corrosion products can induce cracks in the concrete due to the higher volume of rust compared to non-corroded steel, and the combination of these modes of damage may lead to a premature end of the service life of a reinforced concrete structure [1], as described by Tuuti [2]. Preventing and mitigating premature deterioration and repairing and maintaining infrastructure currently account for 3.4% of global GDP, especially in developed countries. These costs could increase 3–6 times by 2060 and represent a significant economic challenge [3].

Chloride diffusion is the first parameter to be evaluated for corrosion protection and prediction of reinforced concrete service life [4]. It is well known that chloride diffusion depends on the permeability and chloride binding capacity (P_{cb}) of concrete. Chloride binding capacity is the ability of cement to remove Cl^- anions from the pore solution and: i) chemically bind them by forming chloride-containing phases including Friedel's and Kuzel's salts, and ii) partially adsorb them physically on the outer surface of the high-surface area binding gel phases (e.g. calcium silicate hydrate (C–S–H) in the case of Portland cement), thus hindering diffusion deeper into the concrete [5,6]. In a conventional cementitious binders, these parameters are mainly influenced by the water-binder ratio, the chemical composition of the cement, and the presence of any supplementary cementitious materials (SCMs) [4,7].

The demand for durable building materials has become a compelling environmental issue due to the CO_2 emissions associated with the production of ordinary Portland cement (OPC) for repair or replacement of damaged structures as well as for new structures. Alkali-activated materials (AAMs) based on fly ash and/or blast furnace slag can provide high durability properties at an emissions reduction level of up to 60% compared to Portland cement [8]. However, the knowledge of Cl^- anion diffusion in AAMs is still limited, with various conflicting results existing in the literature. Moreover, findings from studies of OPC or even blended cements cannot be directly applied to AAMs because of the differences and complexity of this system. One of the main differences is the

subordinate role of the water/binder ratio in defining chloride diffusion in AAMs compared to OPC, which has been demonstrated in several studies of AAMs [9–11].

The type of aluminosilicate powder used as precursor is the most important parameter controlling the properties of AAMs. On this basis, AAMs can be divided into: i) high Ca systems, usually alkali-activated slag, in which the main reaction product is a calcium aluminosilicate hydrate (C-A-S-H) type gel, and ii) low Ca systems, usually alkali-activated fly ash or metakaolin, in which the main reaction product is a three-dimensional alkali aluminosilicate hydrate (N-A-S-H) type gel [12]. Alkali-activated slags have shown similar or lower chloride diffusion compared to OPC, mainly due to their finer porosity [10,11, 13] and high tortuosity, which mainly comes from the C-A-S-H gel [14]. Moreover, hydrotalcite-type and zeolite-type phases that form within AAMs were identified as crucial hosts for the chemical incorporation of Cl^- anions from the pore solution into the crystal lattice, analogous to the role of Friedel's salt in OPC [15–18]. This chemical binding was found to provide a higher chloride binding capacity than could be provided by physical adsorption on C-A-S-H gel [19].

Alkali-activated fly ash has shown lower resistance to chloride diffusion compared to alkali-activated slag due to its higher porosity [17,20,21]. Nevertheless, the three-dimensional structure of the N-A-S-H gel provides a higher binding capacity than the C-A-S-H gel due to its larger surface area [22–24]. In some studies, blended systems containing both alkali-activated fly ash and slag have shown higher chloride binding capacity [17], in addition to lower porosity [25].

Another parameter of crucial importance in defining chloride transport in AAMs is the composition and concentration of alkali activators used, as they drastically affect the degree of reaction, and thus pore refinement and hydration products [26,27], which can lead to an increase in binding capacity [22,23]. Ye et al. [15] have shown that the use of a solid alkali activator based on CO_3^{2-} can yield a higher chloride binding capacity despite its relatively low reactivity. On the other hand, Na-silicate activation provides lower porosity and a more homogeneous paste, resulting in a lower chloride diffusion coefficient [28–30].

From the reviewed literature, the crucial parameter for understanding chloride transport in AAMs is the microstructure of AAMs, especially the pore structure. The objective of this study is to evaluate the influence of the microstructure and chloride binding capacity (P_{cb}) of alkali-activated mortars on their chloride transport properties. Three different AAM mortars were prepared with differing Ca contents by varying the blend of precursors (siliceous fly ash and ground granulated blast furnace slag), and for all three types of precursors mixes with three different doses of activator were prepared. Chloride diffusion was evaluated using standard methods of bulk diffusion (according to NT BUILD 443) and accelerated migration (according to NT BUILD 492). Microstructure of mortars was investigated using mercury intrusion porosimetry (MIP), scanning electron microscopy (SEM), X-ray computed microtomography (μ-CT), and X-ray powder diffraction (XRD). The results will provide an overview of the predominant mechanisms affecting chloride diffusion, and insight into the reliability of the techniques developed for OPC when applied to testing chloride transport in alkali-activated materials.

2. Materials and methods

2.1. Materials

A commercial ground granulated blast-furnace slag (BFS_E) supplied

by Ecocem (Moerdijk, Netherlands), and a siliceous fly ash (FA_P) from coal-fired power plant supplied by Holcim (Plomin, Croatia) were used as solid precursors for mortar preparation. Table 1 shows the chemical compositions of the precursors (expressed as oxides), obtained by X-ray fluorescence spectroscopy. Fig. 1 shows the X-ray diffraction pattern of the precursors, with 10% ZnO as internal standard. The amorphous content of the blast-furnace slag was 100%, while the fly ash contains 67.9% amorphous phases, 16.4% mullite (approximately $Al_{2.17}O_{4.89}Si_{0.78}$), 14.6% quartz ($SiO_2$), 2.4% anhydrite ($CaSO_4$) and 1% magnetite ($Fe_3O_4$). The reactivity of these precursors obtained by the R3 test from RILEM TC 267-TRM is 824 J/g for BFE_E, and 300 J/g for FA_P [31].

The particle size distribution (PSD) was determined using a Mastersizer 2000 instrument (Malvern Panalytical, Malvern, United Kingdom) with a wet laser diffraction procedure by dispersing the particles in isopropanol [32]. Table 2 shows the density, characteristic values of particle size distribution and pH of precursors obtained through a leaching method [33]. Fig. 2 shows the cumulative particle size distributions of the precursors. Fly ash shows a bimodal distribution with the majority of particles around 20–30 μm, while blast-furnace slag has finer particles, and the bulk of particles around 10 μm in size. Fig. 3 shows examples of the particle morphologies from SEM - SE imaging. The blast-furnace slag shows angular and irregular particles, while the fly ash particles are characterized by a typically spherical shape.

The precursors were activated with sodium silicate Geosil 34417 supplied by Woellner (Ludwigshafen am Rhein, Germany), with Ms (molar ratio SiO_2/Na_2O) = 1.68, blended with 12.5 M NaOH solution to reach the desired activator compositions. Technical grade sodium hydroxide pellets supplied by Grammol (Zagreb, Croatia) were dissolved in distilled water and mixed to prepare the NaOH solutions, which were allowed to cool for 24 h before mortar preparation.

2.2. Sample preparation

Table 3 summarizes the mix designs of the developed AAMs. Mixes are divided into three categories based on the precursors, to represent high-Ca (labelled SN, based on BFS_E), low-Ca (labelled FN, based on FA_P) and blended system (labelled BN, based on 50:50 BSF:FA). SN and FN systems are pure systems based respectively on blast furnace slag and fly ash, inspired by the mix designs of RILEM TC 247-DTA [34]; while BN is a blended system similar to SN with 50% blast furnace slag and 50% fly ash. For each category three mixes were developed with
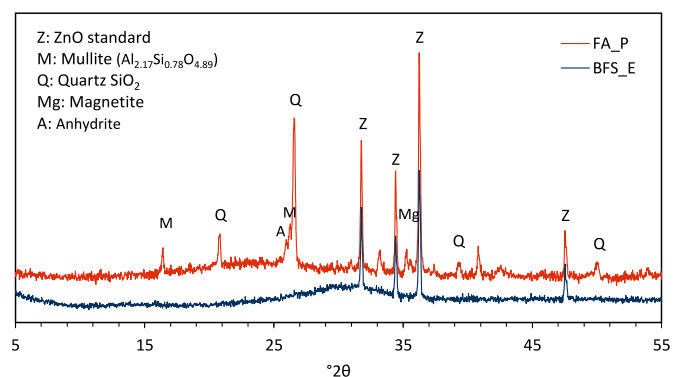
Fig. 1. XRD patterns of the precursor materials.

Table 1
Chemical composition of the precursor materials from XRF.

Oxide composition (mass %)	SiO$_2$	Al$_2$O$_3$	Fe$_2$O$_3$	MnO	TiO$_2$	CaO	MgO	K$_2$O	Na$_2$O	SO$_3$
BFS_E	31.1	13.7	0.4	0.3	1.3	40.9	9.2	0.7	0	2.3
FA_P	57.2	25.1	5.8	0.1	0.9	4.8	1.7	1.5	1.1	0.8

Table 2
Characteristic particle sizes, density and pH of the precursor materials.

	$D_{v,0.1}$, μm	$D_{v,0.5}$, μm	$D_{v,0.9}$, μm	Density, g/cm^3	pH
BFS_E	1.32	4.90	10.61	2.89	11.03
FA_P	0.63	11.50	54.22	2.40	12.24

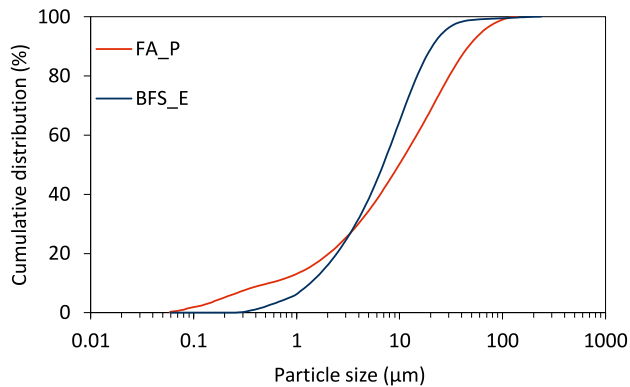**Fig. 2.** Particle size distribution (PSD) of the precursor materials from laser diffraction.

different Na$_2$O%, maintaining a constant waterglass/NaOH ratio. Water/binder ratio was kept constant at 0.45 to achieve a suitable workability for sample casting. The study was performed at mortar scale. The aggregate was local dolomite sand with a particle size range of 0–4 mm. The aluminosilicate powder/aggregate ratio used was 0.33, and was kept constant in all mixes.

AAMs were prepared according to the RILEM TC 247-DTA [34] recommendation: aluminosilicate powder and aggregate were mixed for 60 s, and then again for 6 min while continuously adding activators and water (from the denser solution to the less dense); the mixing was

paused for 60 s and then the mixture was mixed faster for 2 min. Samples were demolded after one day of covered curing and were then sealed cured until the time of testing, by tightly wrapping them with plastic film to prevent carbonation, efflorescence formation and moisture loss.

2.3. Methods

2.3.1. Mortar characterization

The consistence of mortars was measured by a flow table test according to the standard EN 1015-3 [35]. The air content was measured by pressure methods according to the standard EN 1015-7 [36]. The consistence and the air content tests were conducted immediately after mixing at 20 °C. Compressive strength was determined on three 4 × 4 × 16 cm prisms per mix after 7 and 28 days with a loading rate of 2400 N/s, according to the protocols described in EN 196-1 adapted to the analysis of the mortar specimens described in section 2.2 [37].

2.3.2. Chloride diffusion and pH

The resistance of alkali-activated mortar against chloride ingress was measured according to NT BUILD 492, to obtain the non-steady state migration coefficient, D_{nssm} [38] and according to NT BUILD 443, to obtain the apparent chloride diffusion coefficient D_a [39]. The fresh mortar was cast into ⌀100 × 200 mm cylinders. After 28 days of sealed curing, the electrical resistivity of the mortar was measured on the side surface of the cylinder using the Wenner probe, after which the samples were cut into 3 discs of ⌀100 × 50 mm, eliminating the top and bottom sections of each cylinder. For each mix 3 such discs were used for chloride migration test and 3 for diffusion test by ponding.

The non-steady-state chloride migration testing was conducted on three specimens per mix after vacuum treatment with saturated Ca(OH)$_2$ solution, using a PROOVE'it instrument (Germann Instruments, Copenhagen, Denmark) with 0.3 N NaOH as anolyte solution and 2 N NaCl as catholyte solution. The test was carried out applying a constant voltage of 40 V for BN3 and SN3 for 24 h and 10 V in FN9 for 6 h, as described in NT BUILD 492. An important parameter for this test is the
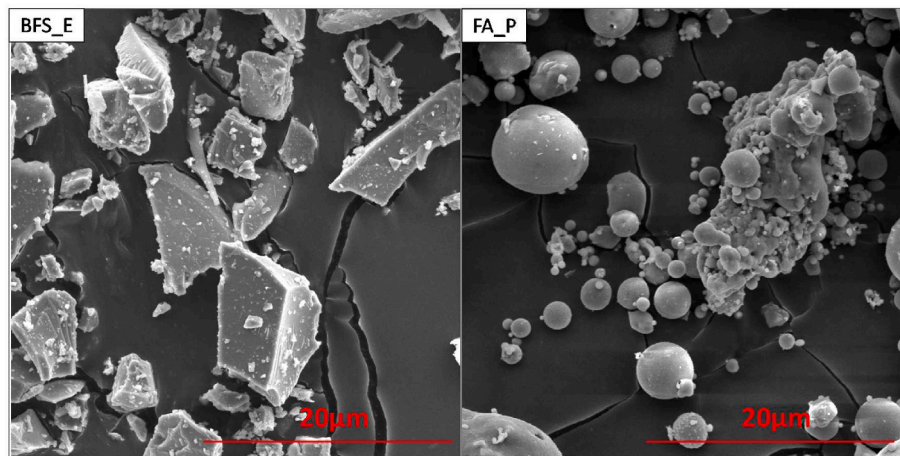

Fig. 3. Micrographs (SEM - SE) of the precursor materials used.

Table 3
Mix designs of the mortars developed in this study.

Mass (%)	SN3	SN5	SN7	BN3	BN5	BN7	FN5	FN7	FN9
BFS_E	87.7	81.9	76.5	41.1	38.4	35.8	–	–	–
FA_P	–	–	–	46.6	43.5	40.6	79.3	73.2	68.7
NaOH[a]	7	10.3	13.5	7	10.3	13.5	5.1	6.6	7.7
WG[a]	5.3	7.7	10.1	5.2	7.7	10.1	15.5	20.1	23.5
SS/SH	0.66	0.66	0.66	0.66	0.66	0.66	2.71	2.71	2.71

[a] The activator content refers to the sum of liquid and solid components.

chloride concentration at which the colour changes (c_d). The NT BUILD 492 recommends a value of 0.07 N as c_d for OPC concretes. However, for AAMs $c_d = 0.21$ was applied [40] to take into account the higher concentration of hydroxide ions (i.e., higher pH value) usually present in these systems, which changes the reaction equilibria that result in formation of AgCl or Ag_2O, and thus also influences the concentration of chloride ions at the critical point (visible penetration front) which is taken as c_d. Thus, the fact that alkali-activated materials have a different chemistry of pore solution, which is not considered in the NT BUILD 492 method, is accommodated by a difference in the c_d parameter.

The chloride penetration testing according to NT BUILD 443 was performed on three specimens per mix by immersing them in 165 g/L NaCl solution. Before exposure to chloride solution, samples were vacuum treated in saturated $Ca(OH)_2$ solution and coated with thin epoxy layer leaving one face free to allow unidimensional chloride ingress. At the end of 35 days of exposure, the grinding was performed with a Germann Instruments Profile Grinder (Copenhagen, Denmark). The total (acid-soluble) and the free chloride (water-soluble) were calculated from the powder extracted at different depths, to estimate the apparent chloride diffusion coefficient (D_a) as average of two specimens per mix. The total chloride was measured according to EN 14629 [41]: 5 g of powder were dissolved into 100 mL of distilled water and stirred to remove any lumps. Then, 10 mL of 5 M HNO_3 acid solution and 4 drops of H_2O_2 (to avoid contributions from reduced sulfur species) were added and continuously stirred and heated until boiling. Total chloride content was measured by 0.1 M $AgNO_3$ titration using a TitroLine 5000 (SI Analytics). The chloride profile of each sample was then plotted, to be used for apparent chloride diffusion coefficient determination. For determination of water-soluble chloride, 3 g of powder were dispersed into 30 mL of distilled water and stirred and heated until boiling. After boiling, the samples were stored at 20 ± 1 °C for 24 h and then vacuum filtered using Ahlstrom-Munksjö (Helsinki, Finland) filter papers with a pore size of 3-2 μm in a Buchner funnel and suctioned filtration flask. The filter paper, funnel and flask were rinsed with distilled water [42]. The final solution was dissolved into 80 mL of distilled water, 2 mL of 5 M HNO_3 solution and 1 mL of H_2O_2, while it was continuously stirred. Then, the chloride content of solution was measured according to the protocols of EN 14629 [41].

The powder extracted from the discs used in the diffusion tests was additionally used for pH measurement to evaluate the leaching effect. The pH was through the ex-situ leaching by dissolving 3 g of powdered mortar in 30 mL of distilled water. The solution was stirred during the first 5 min and then stored at 20 ± 1 °C for 24 h and then vacuum filtered using Ahlstrom-Munksjö (Helsinki, Finland) filter papers with a pore size of 3-2 μm in a Buchner funnel and suctioned filtration flask. The pH was measured with Lab 850 SCHOOTT Instrument (Hattenbergstr, Germany). The pH of the obtained leachate solution was deemed to be an approximation of the pH of the mortar pore solution, based on the experience of Räsänen and Penttala [33]. However, leaching of powder likely underestimates hydroxide ion concentration because of the dilution effect and the absence of buffer effect from the absence of $Ca(OH)_2$ in AAMs [43]. Nevertheless, in the present study this approximated value was used as a relative, rather than absolute value, to follow the trend of pH between different systems and during exposure to chlorides.

2.3.3. Microstructural characterization

X-ray diffraction (XRD) analysis was applied to paste specimens with same binder mix design as the mortars, and exposed to the same environmental conditions. The paste was finely ground in an agate mortar. The powder was mixed with ZnO used as internal standard for amorphous phase quantification with a ratio of 9:1, and placed in a front-loading sample holder. Data were collected using a Bruker D8 DISCOVER diffractometer (Billerica, USA) with Cu-Kα radiation generated at 40 mA and 45 kV. Specimens were scanned from 5 to 55° 2θ at a step size of 0.2° 2θ. The scan results were interpreted using the software Highscore Plus for phase identification. Phase quantification was carried out with the Rietveld method using ZnO as internal standard.

Mercury Intrusion Porosimetry (MIP) was used to provide information regarding the pore size distribution and pore volume of the mortars and surface area, in the pore size range from 360 to 0.006 μm [44]. MIP tests were performed on samples of approximately 1.5 cm³. The specimens were crushed in small pieces and immersed in isopropanol, and after 7 days they were vacuum dried. An Autopore IV 9505 instrument was used for the MIP measurement, with a maximum pressure of 208 MPa. The pore diameter was derived using Washburn's law (Eq. (1)):

$$D = \frac{(-4 \cos \theta) \bullet \gamma}{P} \tag{1}$$

where D is the pore diameter (μm), θ is the contact angle between the fluid and the pore mouth (130°) [45], γ is the surface tension of the fluid (485 mN/m) [32], and P is the applied pressure to fill up the pore with mercury (MPa). The data obtained from MIP were used to determinate total porosity, effective porosity, critical pore radius entry (r_{crit}) and threshold pore entry radius (d_{th}), Fig. 4.

The total porosity is quantified from the maximum intrusion, and the effective porosity was determined by the difference between the total intruded and extruded Hg to avoid the "ink-bottle" effect and overestimation of finer pores [46,47].

The threshold pore entry radius (r_{th}) was obtained through the *tangent method*, where r_{th} is the minimum radius that is geometrically continuous throughout the whole sample, graphically obtained as the intersection between the two tangents drawn to the cumulative curve [32]. According to the cumulative curve shape obtained in most of the samples, it is possible to use the tangent method to identify two different r_{th} values: a primary r_{th} indicated as $r_{th,1}$, which represents the first percolation process; and a secondary r_{th} indicated as $r_{th,2}$, which represents the virtual size after the second percolation process has been reached. This secondary threshold diameter provides information about the presence of choke points [48]. However, the critical pore radius entry (r_{crit}) is preferred to r_{th} because it is mathematically calculated by the inflection point of the main intrusion step and it is the pore size where the steepest slope of the cumulative intrusion curve is recorded [32].

Microstructural analysis was performed using a Mira II LMU scanning electron microscope (SEM). The specimens were cold mounted in resin EpoFix under vacuum. After 24 h, specimens were manually ground with 400, 600, 800 and 1200 grit papers. The resulting surfaces were then polished using 9, 3 and 1 μm diamond suspensions. The polished samples were Cr-coated ot prevent charging.

X-ray computed microtomography analysis was performed using an Xradia MicroXCT-400 (Xradia, Pleasanton, California, U.S.), on a randomly selected fragment of material representing the bulk mortar sample. The X-rays were generated at 60 kV and 100 μA, for all the samples. Using a high precision rotating stage, 986 projection images were taken from different points of view (recorded at different angles during stepwise rotation between 0° and 360° around the vertical axis) with an exposure time of 5 s per projection. Beam hardening was reduced by the presence of an LE#1 filter (removing low-energy X-rays) between the source and the detector. The transmitted images were then detected by an X-ray image detector which consisted of a CCD camera equipped with a 10 × magnification optical objective. The pixel resolution under these conditions was between 1.79 and 2.35 μm, depending on the sample. The tomographic reconstruction was performed using XMReconstructor software. Using the stack of slices obtained in this way it was possible to define the reconstructed volumetric data of the scanned object. Avizo Inspect 3D (version 2019.1) analysis software was used for pore segmentation, quantification, distribution, and visualization of the internal structure. ImageJ 3D was used for pore segmentation, and surface area quantification.

The porosity determination was performed on 3D slice views (planes, XZ, XY and YZ). With appropriate image segmentation, which was based
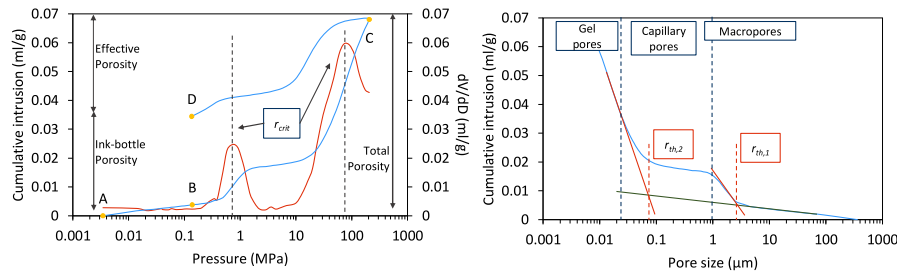
Fig. 4. Graphical representation of total porosity, ink-bottle porosity, effective porosity, and critical pore radius. The line connecting points A-C is the Hg intrusion curve, and the line connecting points C-D is the Hg extrusion curve.

on hysteresis thresholding, the specimen was segmented from the voxel intensity histogram of the greyscale image. The white and grey voxels represent the reaction products, anhydrous aluminosilicate powder and aggregate, and the black voxels are the pores and cracks [49]. The samples were analyzed using two different software platforms for 3D analysis. Firstly, AVIZO 3D was used to segment the picture base on the grey level, applying a watershed to the binary images in order to separate visually the pores from the matrix and aggregate. The term "watershed" comes from the analogy in which the grayscale image is treated as a topographic surface, i.e. the pixel (or voxel) intensity corresponds to the height of the point map [50]. Secondly, the binary images were filtered using a median filter to flatten the picture and remove discoloration, using ImageJ 3D. After this, the pores were separated from the matrix and the aggregates, using thresholding based on the grey level [51].

3. Results

3.1. Mortar characterization

Table 4 shows the fresh and mechanical properties of the mortars. These alkali-activated mortars exhibited a consistency greater than 115 mm in the flow table test, and the consistency increased proportionally with the activator content, since the higher pH of the solution leads to an increase in the initial dissolution and the silicate constituent of the activator also has a plasticizing effect [10,52]. For systems containing fly ash (BN and FN), the air content also increased with increasing activator content, while for slag-based systems (SN), the air content decreased with increasing activator content. Compressive strength increased with increasing curing time and activator content in SN and FN systems, while blended systems showed no evident differences with different activator contents, contrary to the results in the literature [10, 53]. When moving from a high Ca system to a low Ca system, the overall compressive strength decreased, as has already been shown [54], due to the lower reactivity of fly ash than slag.

Table 4
The fresh and mechanical properties of the mortars tested.

Mix	Consistency (mm)	Wet density (kg/m³)	Air (%)	Compressive strength (MPa)			
				7 Days		28 Days	
SN3	165	2299	2.8	36.0	±1.3	47.7	±0.8
SN5	198	2310	2.4	33.2	±2.0	49.0	±2.0
SN7	253	2323	2.0	45.0	±0.5	54.9	±1.4
BN3	115	2257	2.1	24.5	±0.1	38.0	±0.9
BN5	175	2260	2.4	24.6	±0.1	38.4	±1.5
BN7	245	2251	2.5	26.5	±0.5	39.9	±0.4
FN5	228	2221	2.4	0.2	±0.2	6.0	±0.6
FN7	265	2200	2.6	0.3	±0	15.4	±0.3
FN9	300	2149	2.8	5.3	±2.5	25.9	±3.0

3.2. Chloride diffusion, chloride and pH profiles

Fig. 5 shows the profiles of total chloride content after 35 days of exposure to a 16.5% NaCl solution. SN and BN samples showed a similar trend, where chloride decreased dramatically in the first 10 mm depth after a high chloride concentration was calculated at the surface (C_s). In contrast, the low Ca FN systems showed a more homogeneous and uniform chloride distribution across the profile to 20–25 mm and a smaller difference between the chloride content at the surface (C_s) and the deeper layers. The free chloride content profiles showed a similar trend to the total chloride content, but with visibly lower concentrations. The chloride concentration reaches 0% at 5 mm depth in almost all mortars containing slags.

Fig. 5 also shows the pH profiles of the mortar samples tested after chloride exposure, as well as the initial pH after 28 days of curing before chloride exposure (indicated by a green dot symbol). The pH provides information on the leaching of the pore fluid and/or binder constituents from the mortar under the exposure conditions. Despite the short exposure period (only 5 weeks) and the pretreatment of the mortar (saturation with Ca(OH)$_2$ solution), all systems showed a pH drop at the surface after exposure to chlorides, which can be attributed to loss of pore solution alkalinity due to the aqueous exposure [10,55]. The depth of the leached zone was between 5 and 7 mm for SN and BN samples. At depths beyond this, the pH stabilized and reached a value comparable to the pH before aqueous exposure, or even higher for some of the SN samples. In FN samples, no distinct leached zone was apparent from the pH profiles in Fig. 5 within the first 25 mm, but it is entirely possible (considering the relatively low measured pH values) that this entire region has in fact been partially leached during the test.

Overall, the pH before and after aqueous exposure increased with increasing Na$_2$O%. However, FN samples showed a greater pH decrease after the ponding time compared to SNs and BNs, indicating a greater sensitivity of the low Ca systems to the leaching of the pore solution.

The accelerated chloride diffusion coefficient (D_a) was determined by measuring total chloride (*acid soluble method*). Table 5 summarizes the results of fitting the data shown in Fig. 5 by means of a non-linear regression analysis using the method of least squares, omitting the chloride content determined from the exposure surface layer in the regression analysis. The results show that the activator content and the type of precursor affected the resistance to chloride ingress. Increasing the activator content hindered chloride ingress, samples containing blast furnace slag behave similarly while the low Ca systems resulted in low resistance to chloride ingress, consistent with previously reported results for blended slag-fly ash AAMs at different ratios [54]. The apparent chloride diffusion coefficient for high- and moderate-calcium AAMs was low compared to a conventional OPC concrete with similar water-solid ratio [11,56]. The high diffusion coefficient of FNs is mainly due to the low amorphous content of FA_P and the consequent lower reactivity, as well as the lack of space-filling character of the N-A-S-H gel that forms as a reaction product, resulting in a more permeable system [57].

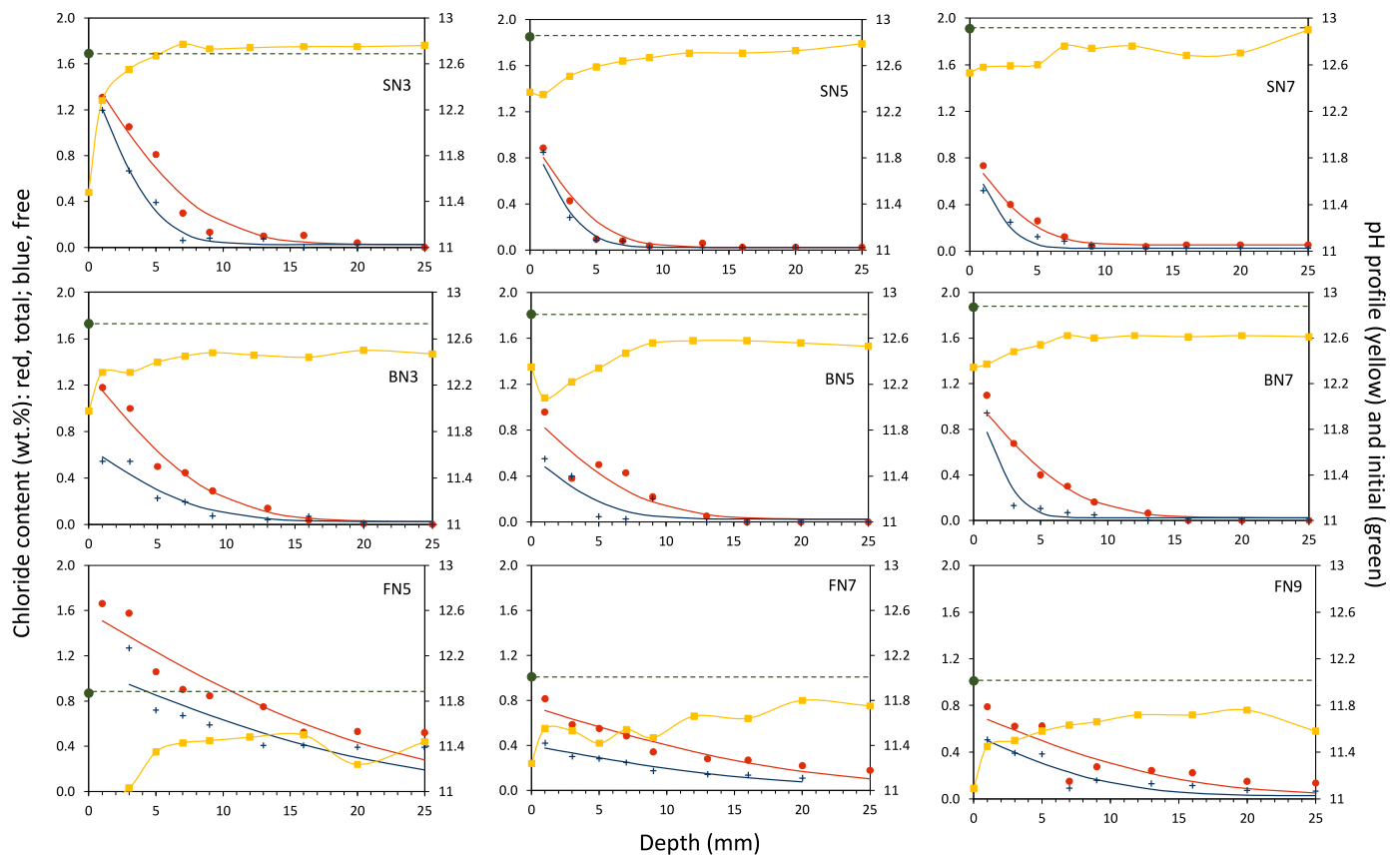Fig. 6A shows the correlations between the apparent chloride

Fig. 5. Total (red dots) and free (blue crosses) chloride profiles with fitting curve, pH profiles (yellow squares) of alkali-activated mortars after ponding and pH at 28 days before ponding (green dots and dotted line). (For interpretation of the references to colour in this figure legend, the reader is referred to the Web version of this article.)

Table 5
Surface resistivity and chloride diffusion coefficient according to NT BUILD 443 and 492 after 28 days.

Mix	NT BUILD 443		NT BUILD 492	Surface resistivity
	D_a	C_s (%)	D_{nssm}	(kΩ·cm)
	(10^{-12} m²/s)		(10^{-12} m²/s)	
SN3	7.2	1.51	1.6 ± 0.3	57.6
SN5	3.0	0.98	1.3 ± 0.2	36.6
SN7	2.5	0.82	0.6 ± 0.2	27.6
BN3	8.2	1.3	2.2 ± 0.5	76.6
BN5	7.0	0.93	1.4 ± 0.4	57
BN7	6.0	1.08	0.7 ± 0.07	37.3
FN5	53	1.58	–	5.8
FN7	40	0.75	176 ± 25	5.1
FN9	23	0.73	174 ± 9	2.9

diffusion coefficient and the non-steady-state migration coefficient for alkali-activated mortars studied. Although the results indicate a similar trend, it is not possible to define a precise correlation between these two tests applied to AAMs with different precursors, as previously shown [54,57,58]. The data from the accelerated NT BUILD 492 test underestimated chloride diffusion for high and medium- Ca systems and overestimated it for low- Ca systems, compared to the ponding test. This underestimation is in contrast to literature results for OPC and other cementitious systems, where NT BUILD 492 generally overestimated chloride diffusion compared to ponding [7]. In any case, RILEM TC 247-DTA [57] has already reported unclear correlation for alkali-activated materials between diffusion coefficient obtained according to the NT BUILD 443 and migration coefficient obtained according to the NT BUILD 492.

Fig. 6B shows the correlations between the apparent chloride diffusion coefficient and surface resistivity. Surface resistivity has already shown good correlation with sorptivity of the alkali-activated mortar [54], and the more highly permeable FN samples do show a low resistivity as expected. However, for the Ca-richer samples (SN and BN series), increased Na_2O content reduced surface resistivity in all systems, while also reducing the D_a. This trend may be connected to the different chemical composition of the pore solution in AAMs. Indeed, Lloyd et al. [59] demonstrated that the pore solution of AAMs showed higher concentrations of alkali (Na^+, K^+) and OH^- anions than OPC, which depends on activator content. The higher content of alkali and OH^- anions (visible in this study through the higher pH values presented in Fig. 5) may increase the conductivity of the pore solution. In fact, low Ca systems showed lower resistivity compared to high Ca systems due to the faster consumption of alkali in the reaction process at lower calcium content [60]. Thus, the trend in resistivity is contrary to the accepted correlation for OPC and blended systems from the literature [7,61], suggesting that in the case of AAMs, porosity, pore interconnectivity, and chloride binding capacity have a greater effect on preventing chloride diffusion than the chemical composition of the pore solution [7]. Moreover, the results show that a clear correlation between Ca content and surface resistivity is not possible.

3.3. Microstructural characterization

Fig. 7A–F shows the cumulative and differential curves of alkali-activated mortars after 28 days of curing, as determined by MIP. From the cumulative curve, it is possible to divide the porosity into three different groups based on the pore size distribution, based on previous observation in AAMs [20,47]: gel pores below 0.015 μm (which have no
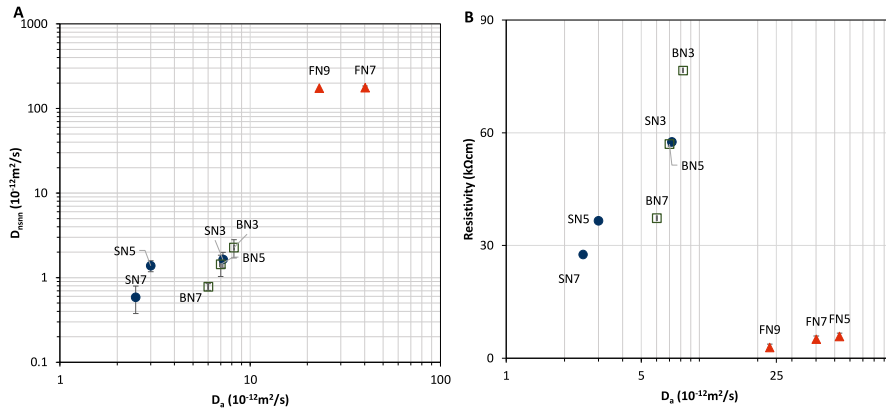
Fig. 6. Correlations between measured transport parameters: (A) non-steady state migration coefficient vs. apparent chloride diffusion coefficient; (B) surface resistivity vs apparent chloride diffusion coefficient.
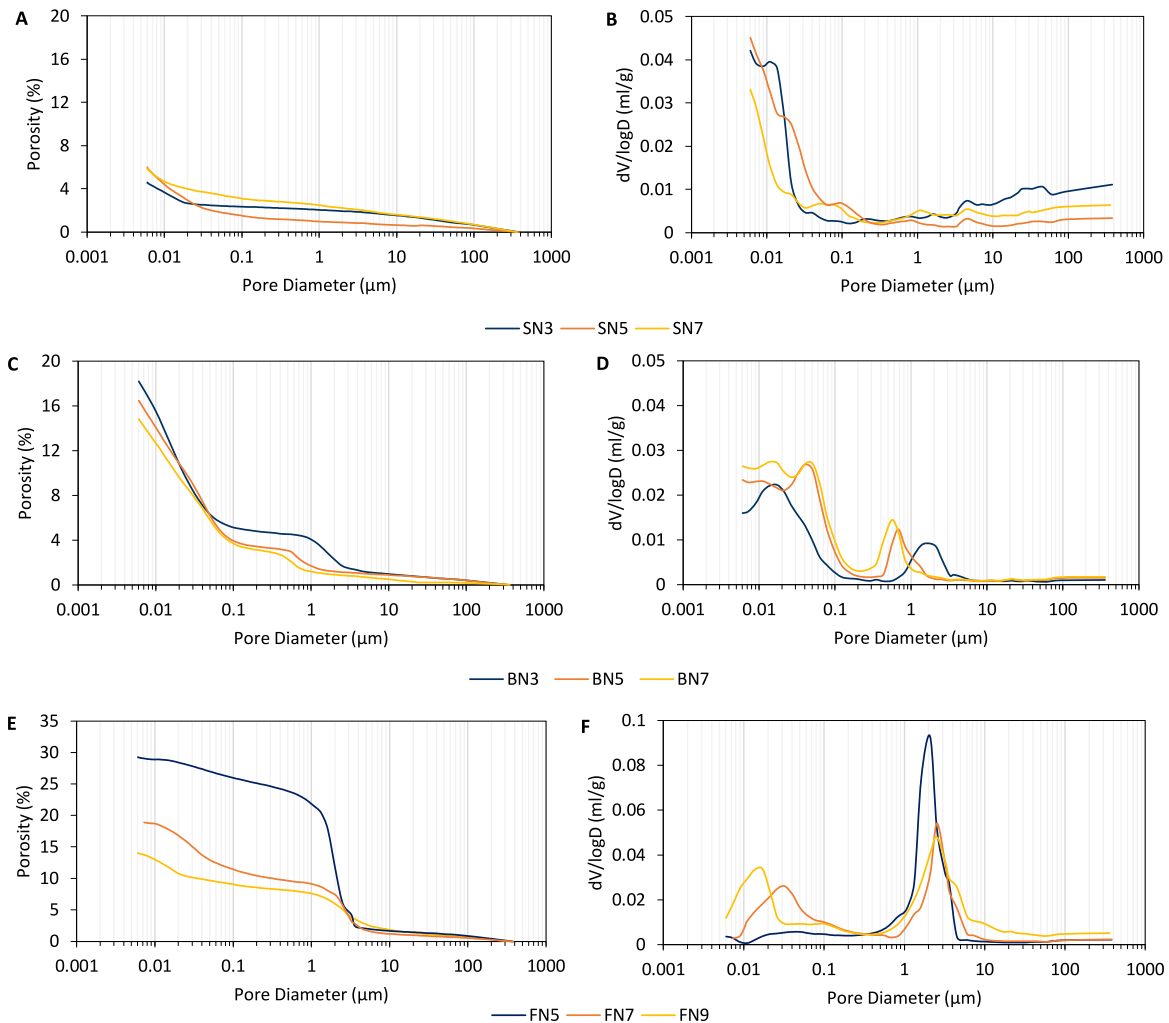

Fig. 7. Pore size distribution cumulative curve and pore size distribution differential curve at 28 days of mortar samples tested: alkali-activated slag (A and B), alkali-activated slag-fly ash (C and D) andand alkali-activated fly ash (E and F). Note that for alkali-activated fly ash, the scale of y-axis is bigger because of the bigger porosity in these systems.

effect on permeability), capillary pores between 0.015 and 1 μm (which affect fluid permeability and mechanical properties [62]), and macropores with a radius ≥1 μm, which mainly affect mechanical properties

[63]. The content of each pore group is summarized in Table 6, while Table 7 shows the threshold pore radius (r_{th}) and the critical pore radius entry (r_{crit}).

Table 6

Porosity and pore size distribution parameters calculated from MIP data for alkali-activated mortars at 28 days.

Mix	Total Porosity (%)	Effective Porosity (%)	Surface area (m²/g)	Gel pores ≤15 nm (%)	Capillary pores 0.015–1 μm (%)	Macropores ≥1 μm (%)
SN3	4.6	1.4	7.9	0.7	1	2.9
SN5	6	1.8	13.9	1.0	2.6	2.4
SN7	5.9	1.2	9.1	0.5	1.6	3.7
BN3	18.2	1.3	34.2	2.7	8.9	6.6
BN5	16.5	1.6	29.3	2.0	10.9	3.6
BN7	14.8	1.8	26.4	1.8	10.1	2.9
FN5	29.2	5	1.5	0.0	7.2	22
FN7	18.9	2.6	12.6	6.6	10.5	1.8
FN9	14	3.1	12.5	1.2	4.5	8.3

Table 7

The critical pore entry radius and threshold pores of the gel and the capillary pores in alkali-activated mortars at 28 days.

Mix	Critical pore entry radius, r_{crit} (nm)		Threshold pore radius, r_{th} (nm)	
	Gel pores	Capillary pores	Gel pores	Capillary pores
SN3	29.4	–	18	–
SN5	23.7	–	28	–
SN7	10.8	–	10	–
BN3	45.4	2322.9	50	2350
BN5	56.6	494.6	80	1050
BN7	57.1	393	90	760
FN5	–	2894.9	–	2500
FN7	45.4	3440.1	61	2850
FN9	19.1	3427.4	24	3600

The alkali-activated slags (SN series) always had a measured porosity of less than 6%, and most pores are in the capillary and macropore range, as confirmed by Fig. 7A–B. Moreover, the SN series show no evident correlation between activator content and porosity. In fact, SN3 has a lower porosity than SN5 and SN7. In SN3 and SN7, almost 50% of the pores are in the macropore range, while SN5 has fewer macropores and more capillary pores. The porosity trend was also confirmed by the r_{th} values in Table 7, while r_{crit} decreases with increasing Na$_2$O content.

Alkali-activated fly ash and blended slag-fly ash systems show double peaks in the differential curves in Fig. 7D–F. This curve shape indicates the presence of a 'choke point', where flattening of the differential curve followed by a steep rise indicates that a relatively high pressure rise was needed to fill a certain pore size range, while alkali-activated slag systems showed only one peak from where it was possible to calculate r_{th} and r_{crit} [48]. For this reason, Table 7 shows only one r_{crit} and r_{dt} for AAS, individuated int the range of gel pores. After the pressure rise, some large pores with narrow throats may be filled and mistakenly estimated to be finer due to the non-homogeneous pore connections. Indeed, pores in cementitious binders are heterogeneous and irregularly connected: mercury reaches the pores in the interior of the sample through a sequence of intermediate pores of different sizes and shapes, which can lead to underestimation of the pore size distribution [64]. This behavior is also described as the 'ink-bottle effect' and represents a biggest limitation of MIP in cementitious materials. In any case, the first peak was located between 0.3 and 3 μm, the second one below 0.1 μm (Fig. 7C–F).

In the BN series of samples, the peak depth, representing the amount of pores, increased with increasing Na$_2$O content, and the width reduced. Indeed, the position of first peak was moved to smaller pore size with higher Na$_2$O%, while the second peak showed the opposite behavior (Fig. 7C–D). This variation is additionally confirmed by the threshold pore radius (Table 7). In the FN samples, the first and the second peaks have more similar trend to the blended systems (Fig. 7E–F). In both systems, increasing Na$_2$O% content caused the

reduction in porosity, as expected due to the higher extent of reaction of the fly ash. However, the effective porosity revealed the opposite behavior due to the high 'ink-bottle effect' produced by fly ash particle dissolution. The low rise in porosity after 1 μm in FN5 may be connected to the fracture of sample during mercury intrusion because of the low strength of mortar.

Porosity was additionally analyzed by μCT on 3D slice views (planes, XZ, XY, and YZ) with appropriate image segmentation, Table 8 (images shown in Appendix A). Here it needs to be highlighted that the data presented were obtained from a single sample per specimen, which induces approximation because of the heterogeneity of materials and the variability of resolution (in particular for BN7). It is therefore that the results presented in Table 8 are given as a first approximation of the porosity detectable by used experimental setup. Only pores with sizes well in excess of 1 μm are measurable by this setup of the technique. In any case, despite their high compressive strengths, SN samples exhibited cracks throughout the specimens (data shown in Appendix A), developed probably during the sample extraction through wire cutters, similar to FN9. Porosity was identified below 0.06% and 0.002%, excluding cracks. The pores identified in SN5 and SN7 were isolated pores. BN showed isolated pores with spherical shape and circularity level higher than 0.84, considered as air bubbles incorporated during the first steps of reaction. Moving from BN3 to BN7, the total porosity increased due to the higher degree of reaction of the more alkaline system. In fact, the higher pH of BN7 dissolved a larger amount of fly ash, leaving empty pores from the spherical shape. However, many pores from fly ash may be unreacted empty fly ash particles, and this may justify the high level of circularity. The majority of the pores were either isolated, or communicate with the external surface only via smaller pores that are not detected by μ-CT. Therefore, the results from μCT could be used in part to explain the results of MIP and provide information about the 'ink bottle effect'.

Fig. 8 shows the pore size distributions of the pores observable in BN3 and BN7 systems.. As the Na$_2$O% content in BNs increased, the average pore size became larger as the higher Na$_2$O% concentration increased the dissolution rate of the cenosphere particles. The results from μCT analysis show the opposite trend compared to MIP results in the same range of pores, but the overall porosity was coherent with the effective porosity of MIP.

Microstructural characterization was also performed using SEM/EDS after 28 days of curing. The microscopic images in Fig. 9 show a comparison of the mortars made from alkali-activated slag-fly ash blends BN3 and BN7 (top images A-D) and alkali-activated slag SN3 an SN7 (bottom images E-H). The BN systems (Fig. 9A–D) are characterized by a matrix based on C-A-S-H and N-A-S-H gel surrounded by irregular angular particles of unreacted slag, ~20–30 μm in size, and spherical particles of fly ash: smaller particles with a diameter of < 10 μm and larger particles with a diameter of > 20 μm. The pores are largely located within partially porous fly ash particles including cenospheres, which can be recognized by their spherical shape, and for this reason are considered as isolated or without connection to the outer surface.

In the alkali-activated slag SN samples, the only visible particles in the binder regions of Fig. 9 (E-H) are the angular, irregular, unreacted

Table 8

Microstructural properties extracted from samples scanned by micro-CT.

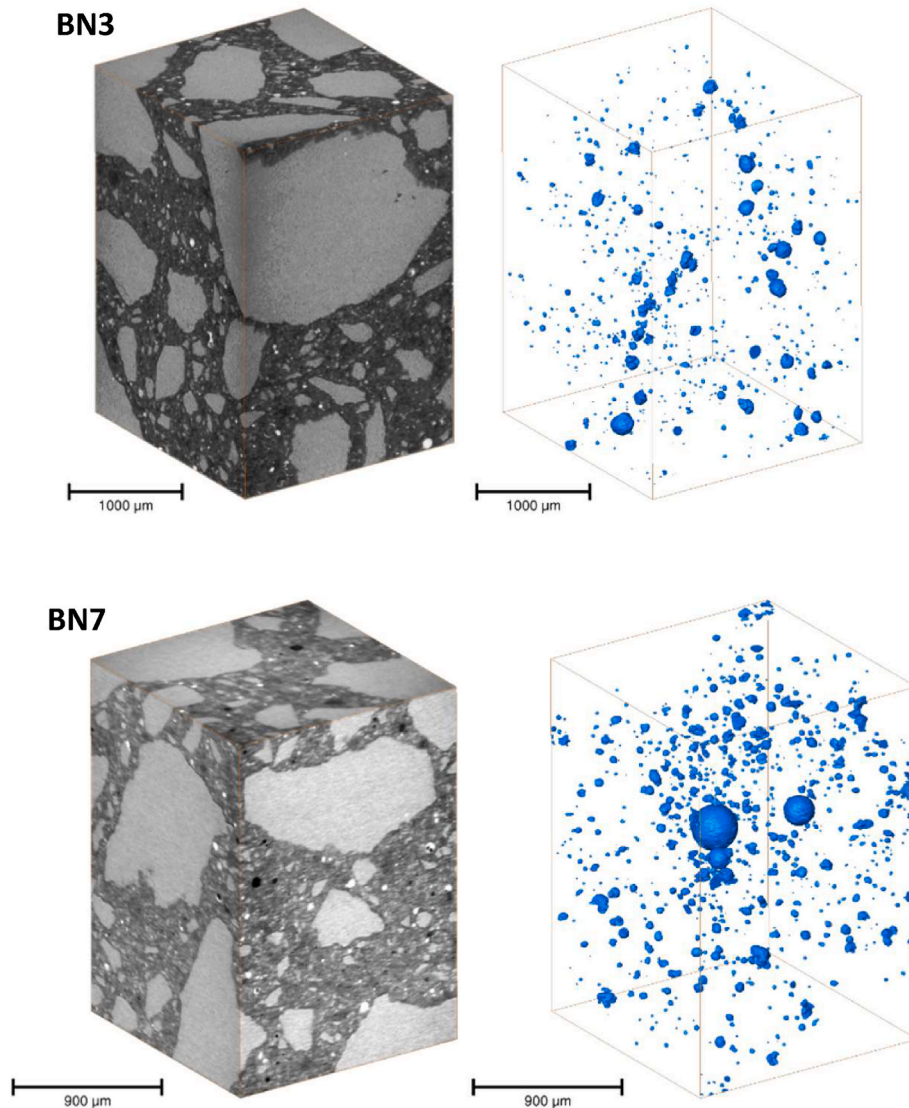| Mix	Resolution (μm)	Measured Pore volume (%)	Total Cracks (%)	Pore perimeter (μm)	Circularity (−)
SN3	1.79	–	0.06	6.5	0.7 ± 0.05
SN5	1.76	0.002	0.048	2.8	0.8 ± 0.03
SN7	1.76	0.002	0.048	3.9	0.78 ± 0.02
BN3	1.73	1.5	–	22.3	0.93 ± 0.01
BN5	1.66	1.9	–	20.9	0.92 ± 0.02
BN7	2.35	3.8	–	9.9	0.84 ± 0.02
FN9	1.76	0.9	0.45	24.1	0.81 ± 0.02

BN3

BN7

Fig. 8. Total scanned mortar volume by micro-CT and model of pores for BN3 with resolution 3.61 μm (top images) and total scanned mortar volume by micro-CT and model of pores for BN7 with resolution 2.35 μm (bottom images).

slag grains surrounded by a matrix based on C-A-S-H gel. The alkali-activated slag has a higher density than the fly ash-slag (BN) binder, and the only visible pores were caused by the air entrapped during mixing. The interfacial transition zone (ITZ) between the aggregate and the paste, as seen in Fig. 9 (B, D, F, H) appears homogeneous and generally has no evident large pores or cracks.

Fig. 10 and Table 9 show the XRD patterns and mineralogical compositions of the alkali-activated pastes after 35 days of ponding. The amorphous fraction represented the major component in all systems and increased with Na₂O% increase. The FN samples consisted of quartz, mullite, and magnetite as unreacted components of the fly ash, while the amorphous phase content increased during curing due to the reaction of the aluminosilicate powder and precipitation of N-A-S-H gel, the main component responsible for both mechanical performance and chloride binding in these samples. On the other hand, systems with high and medium Ca content showed a higher amorphous fraction originating from the blast furnace slag and a weak peak of hydrotalcite, which together with the strength-giving C-A-S-H gel, plays a crucial role in the chemical binding of chlorides [16,17,65]. These results are consistent with the body of literature indicating that chemical binding of chlorides in high-Ca AAM systems is linked to hydrotalcite precipitation [16,29], while low-Ca AAMs were only characterized by chloride adsorption at

the N-A-S-H gel surface [17].

4. Discussion

4.1. Impact of Na₂O concentration on microstructure and chloride binding capacity of AAMs

Alkali concentration (Na₂O%) affects C-A-S-H/N-A-S-H gel precipitation and composition. All mortars studied in this research showed a decrease in chloride diffusion coefficient with increasing Na₂O content. With increasing sodium content, the dissolution rate of the aluminosilicate powder is facilitated and the precipitation of the reaction products is accelerated, leading to a refinement of the pores [66,67]. Consequently, the density of fresh AAMs increases [68] and the chloride diffusion coefficient decreases [69–71]. Moreover, the chloride binding capacity increases with the increase of Na₂O content, because this increase in the dose of the activator leads to an increase in the longer-term degree of reaction, and thus in the gel content, giving opportunities for greater surface adsorption [22].

In support of this line of reasoning, Fig. 11a shows the percentage of bound chlorides (Cl$_b$) in each mortar sample tested here, calculated as the difference between total (Cl$_{tot}$) and free chlorides (Cl$_{free}$) per total
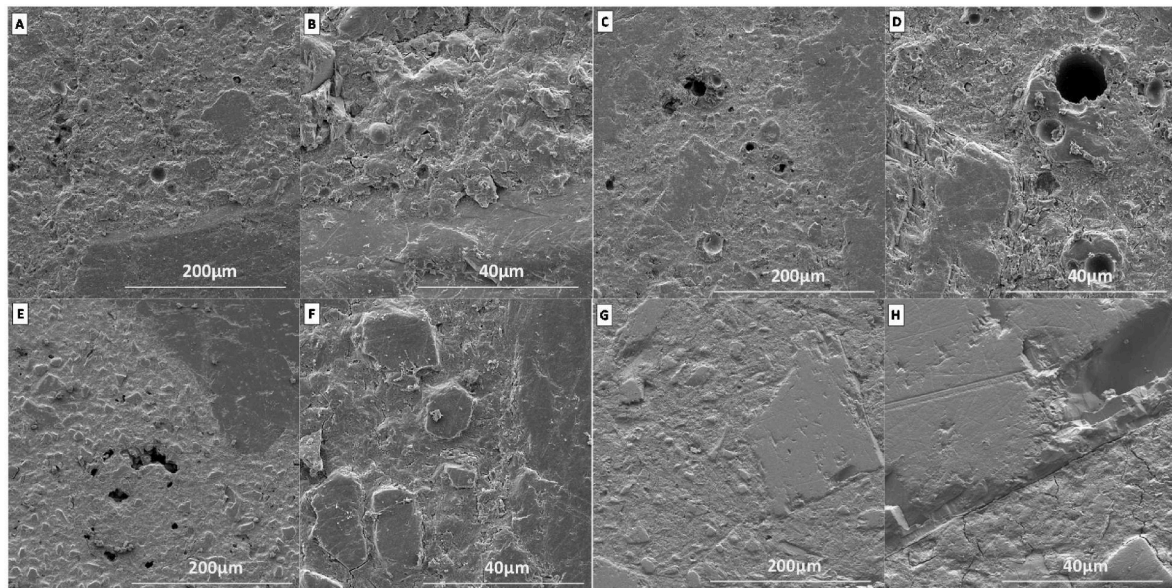
Fig. 9. Micrographs of alkali-activated mortars based on slag and fly ash-slag blend: BN3 (A, B), BN7 (C, D), SN3 (E, F) and SN7 (G, H).
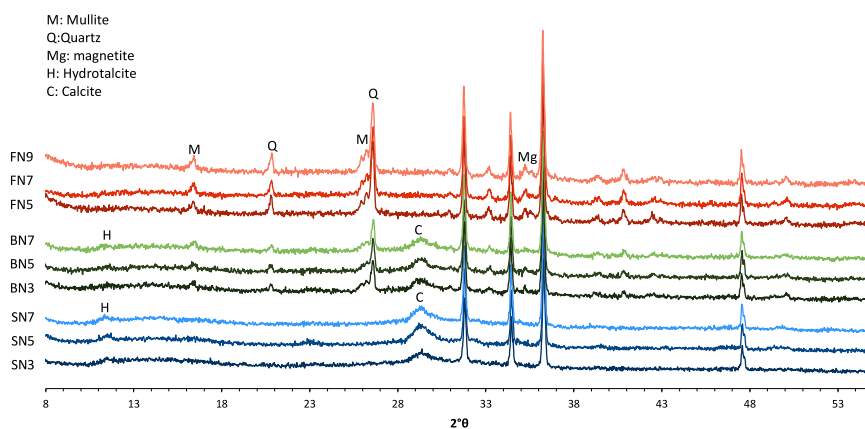

Fig. 10. XRD pattern alkali-activated paste after 35 days of ponding in 16.5% NaCl solution with 10% of ZnO as internal standard.

Table 9
Mineralogical composition of alkali-activated paste after 35 days of ponding in 16.5% NaCl solution.

Reaction products (%wt.)	SN3	SN5	SN7	BN3	BN5	BN7	FN5	FN7	FN9
Calcite	10.4	8.7	8.1	11.2	9.5	7	–	–	–
Hydrotalcite	3.3	5.1	5.3	<1	1	1	–	–	–
Mullite	–	–	–	9.3	10.6	9.5	17.3	15	11.
Quartz	–	–	–	6.4	6.3	5.3	9.3	9.5	9
Magnetite	–	–	–	<1	<1	<1	<1	<1	<1
Amorphous	84.7	84.3	84.4	72.4	72.9	77.5	72.4	73.5	78.5

chloride content. The data show a visible increase in bound chloride with an increase in Na_2O% content. The systems with medium Ca content (BN) showed a higher capacity to bind chlorides, which can be attributed to the high chemical binding effect of the slag-derived hydrotalcite, and the coexistence of C-A-S-H and N-A-S-H gel in blended systems [72], which provide a larger surface area for physical chloride adsorption [17]. However, the effect of Na_2O content on chloride diffusion is not entirely clear, since the higher concentration of OH^- in the pore solution causes a decrease in binding capacity [17] due to competition for the anion binding sites. The results for slag-based systems have shown the importance of chloride binding capacity in preventing chloride penetration: although SN3 had lower porosity, the diffusion coefficients of SN7 and SN5 were lower compared to SN3, due to their increased binding capacity.

Fig. 11b shows the relationship between bound chloride (Cl_b) and mortar pH after 35 days in 16.5% NaCl. The low Ca systems have a visible correlation between pH and Cl_b; with a decrease in pH, the bound chloride content increases. This could be related to the higher exposure of the shallow layer to the leaching of the pore solution, but it also depends on OH^- replacement by Cl^- anions. Systems with high and medium Ca content show similar behavior but have poorer correlation due to the low pH drop in the deeper layer and lower chloride
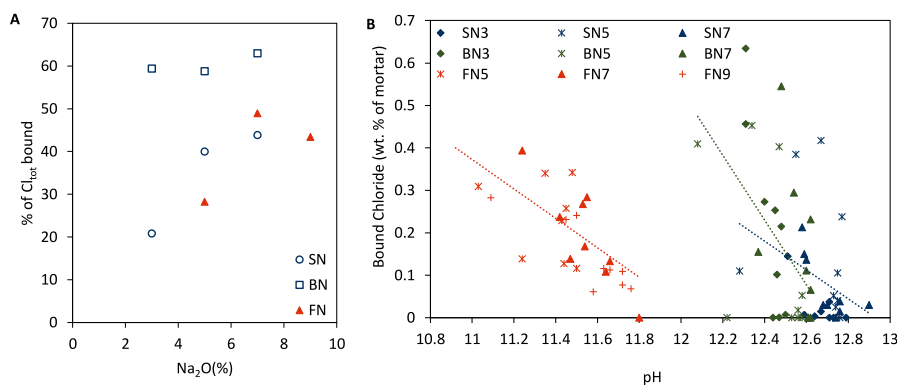
Fig. 11. (a) Percentage of bound chloride from total chloride in AAMs vs. the Na$_2$O% concentration and (b) the correlation between the bound chloride from bulk mortar and pH from leaching after 35 days of exposition in 16.5% NaCl solution.

concentrations.

4.2. Influence of physical and chemical properties of aluminosilicate precursors on pore microstructure and chloride penetration

The chemical and physical properties of the aluminosilicate precursors have a strong influence on the chloride diffusion coefficient. In this study, the particle size of BFS_E and FA _P is similar (Fig. 2), but BFS has lower crystallinity and higher reactivity degree than FA. For these reasons, fly ash takes longer than slag to develop a microstructure and precipitate reaction products [73,74]. This behavior justifies the insufficient strength of fly ash-based system after 7 days of curing and affects its resistance to chloride diffusion. However, different curing conditions may accelerate the reaction kinetics in fly ash-based systems and lead to lower chloride diffusion, as demonstrated by Noushini et al. [58]. The spherical shape of the fly ash particles (Fig. 3) affects the microstructure and crosslinking within the matrix of the AAMs. Indeed, the fly ash particles leaves empty spherical pores with a diameter of 10–20 μm, visible from the μ-CT, connected to the outer surface by pores smaller than 5 μm, which leads to a misleading pore size distribution in MIP [47], these pores are due to both the dissolution of spherical particles and hollow particles with no connection to the outside [30].

Particle shape has an important influence on microstructure, especially pore connectivity and surface area. However, the chemical composition is the main aspect affecting the behavior of the aluminosilicate precursor in AAMs. Slag-based systems are indeed Ca-rich binders with C-A-S-H gel as the main reaction product, while low Ca fly ash is rich in Al and Si and N-A-S-H gel as the main reaction product. The reaction products affect the microstructure and binding capacity of the systems. C-A-S-H gel leads to pore refinement and increases tortuosity, resulting in a decrease in chloride diffusion [11,14,54,75]. N-A-S-H gel, on the other hand, has a larger surface area that allows higher physical adsorption of chloride anions [6,17]. In addition, the Mg content of the slag favors the precipitation of hydrotalcite as a reaction product that takes up chlorides from the pore solution and combines them with its mineralogical lattice [16,28,76]. Blended systems based on fly ash and slag have a higher chloride binding capacity because the coexistence of C-A-S-H and N-A-S-H gel leads to high physical chloride adsorption on the N-A-S-H gel surface and to pore refinement and high tortuosity of C-A-S-H gel, while the Mg content leads to a negligible amount of hydrotalcite. Despite the small amount of hydrotalcite formed in the BN binders which contain 50% fly ash, the blended systems showed similar chloride diffusion resistance to pure slag systems regardless of the double porosity. This indicates the importance of pore connectivity and the influence of physical adsorption in addition to chemical binding, in defining chloride binding capacity in AAMs.

4.3. Impact of pore microstructure on chloride penetration

Sui et al. [77] have demonstrated the importance of microstructure to prevent chloride transport in cementitious materials. In AAMs, porosity and pore structures have a strong influence on the chloride ingress. However, the total porosity does not show any visible correlation with the chloride diffusion coefficient, even if only the region of capillary pores is considered, in contrast to the results in the literature [75]. This behavior is evident when AAMs based on different precursors are compared. The porosity and pore size distribution from MIP may be miscalculated because the connectivity and shape of the pores are not considered. Micro-CT data reveal the complex structure of systems containing fly ash. They are characterized by macropores connected to the outer surface by finer pores, which may be partially presented as a 'choke point' in the differential curve of MIP. The double peaks in the differential curve of the pores indicate the penetration of mercury into macropores through gel and capillary pores. This phenomenon is known as the 'ink bottle effect' and has major implications for fly ash-based materials [20,46]. Slag-based systems showed extremely fine porosity due to C-A-S-H gel precipitation, which is confirmed by SEM micrographs, where slag-based systems are denser than others and the majority of pores are isolated or poorly connected. In addition, Provis et al. [14] have shown that as the slag content increases, the tortuosity increases, leading to a decrease in diffusion properties.

From the MIP diagrams, the threshold value (d_{th}) and the critical
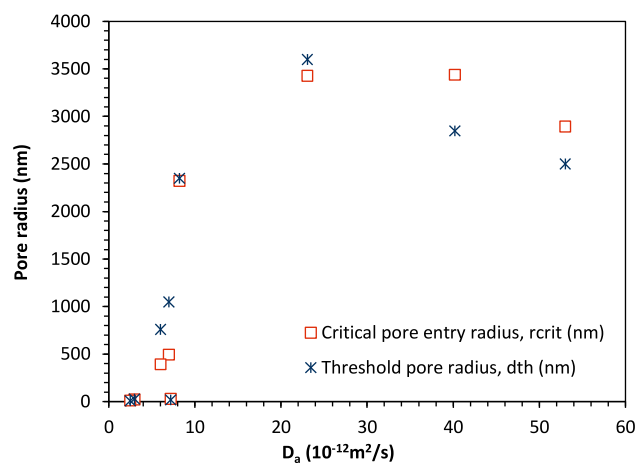

Fig. 12. Correlation between chloride diffusion coefficient (D_a) and microstructure properties from MIP critical pore radius entry in nm and threshold pre radius in nm.

pore radius (r_{crit}) can be obtained, and Fig. 12 shows a comparison between these and the D_a values for the samples studied. These parameters show a good Spearman correlation with the chloride diffusion coefficient: 0.9 for r_{crit} and 0.88 for d_{th}.

Guo et al. [6] have demonstrated the correlation between binding capacity and the surface area, especially when physical adsorption is important. Fig. 13 shows the correlation between the pore surface area and the amount of chloride bound, expressed in mg/g, with a strong coefficient of correlation (0.9). The systems FN5 and FN7 are excluded from the linear correlation because they show out-of-range data due to their lower reactivity, resulting in a very low strength and potential cracking of the sample during MIP testing. This correlation shows the crucial role of physical adsorption at the C-A-S-H/N-A-S-H gel surface. However, the surface area is extracted from MIP measurements, which is an unconventional technique for this purpose because mercury does not penetrate gel pores finer than 6 nm and its high surface tension does not allow the surface area to be measured near small corners [32]. For these reasons, the surface area will be underestimated.

5. Conclusion

Comparing methods used in this study for evaluating chloride penetration originally designed for OPC systems and here used for AAMs, it can be concluded that chloride migration method slightly underestimates the penetration of chlorides in a well-designed system based on slag and slag-fly ash. On the other side, for a poor performing system based on fly ash, chloride migration method significantly overestimates the penetration of chlorides. Furthermore, it is not possible to define a correlation between the surface resistivity and chloride diffusion that is valid for all systems. The difference in the relationship between accelerated diffusion and migration has highlighted the importance of the chemical and physical properties of the precursors used. Alkali-activated slag showed better resistance to chloride diffusion due to the high degree of C-A-S-H gel polymerization and fine porosity, resulting in a relatively dense microstructure and complex pore interconnectivity. Alkali-activated fly ash, on the other hand, showed poor protection against chloride penetration and high porosity, which can be attributed to the low reactivity of the fly ash used and the limited space-filling character of the N-A-S-H gel formed at the studied conditions. However, it must be emphasised that in the present study fly ash with low reactivity was used, activated with a smaller amount of activator and cured at room temperature. Therefore, any conclusions regarding alkali-activated fly ash are limited to the special case presented in the present study. In any case, the low connectivity of large pores originating from the fly ash to the outer surface, and the combined effect of the chloride binding capacity of C-A-S-H and N-A-S-H gel, make fly ash-slag blended systems a good way to reduce the dependence on blast furnace slag by using less reactive materials, even at low activator levels.

The activator dose, represented as Na$_2$O%, plays a crucial role in the development of fresh and mechanical properties and chloride resistance. However, it has limited effects on microstructural properties, especially in terms of overall porosity. There are also important limitations associated with using MIP and μCT when studying AAMs. Nevertheless, the microstructural study here showed a visible correlation between the chloride diffusion coefficient and the critical pore radius, r_{crit}, obtained from MIP. This correlation has shown some limitations in previous
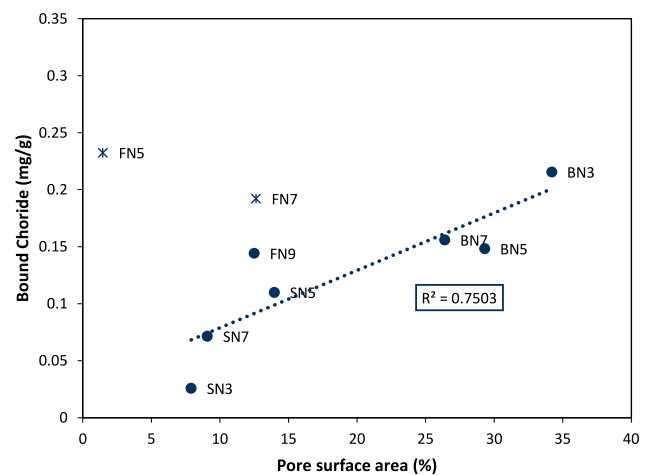

Fig. 13. Correlation between pore surface area from MIP and bound chloride in mg/g.

studies when used for different binders, while in the present research it showed a strong correlation regardless of the type of precursor used. The critical pore radius represents the point of highest pore connectivity and path continuity in the binder matrix and, therefore, can be considered a key microstructural parameter that influences chloride diffusion.

Finally, the chloride profiles showed a visible binding capacity in AAMs. The amount of bound chlorides showed a positive correlation to pore surface area. Moreover, the low amount of AFm phases indicated the main contribution of the C-A-S-H/N-A-S-H gel to the chloride binding capacity.

Future research is clearly needed to understand the behavior of a wider range of precursors in terms of chloride penetration resistance and the influence of microstructure.
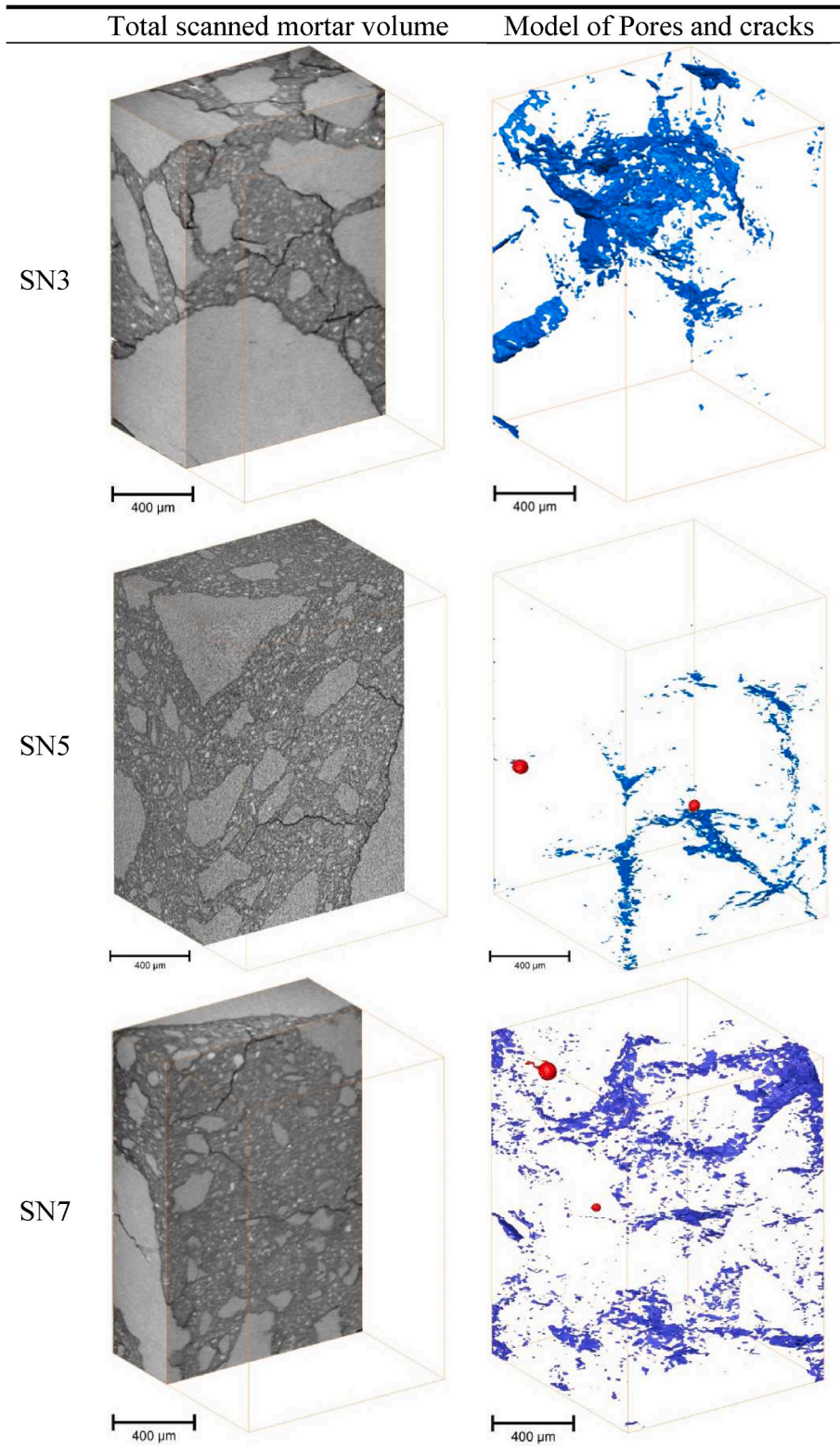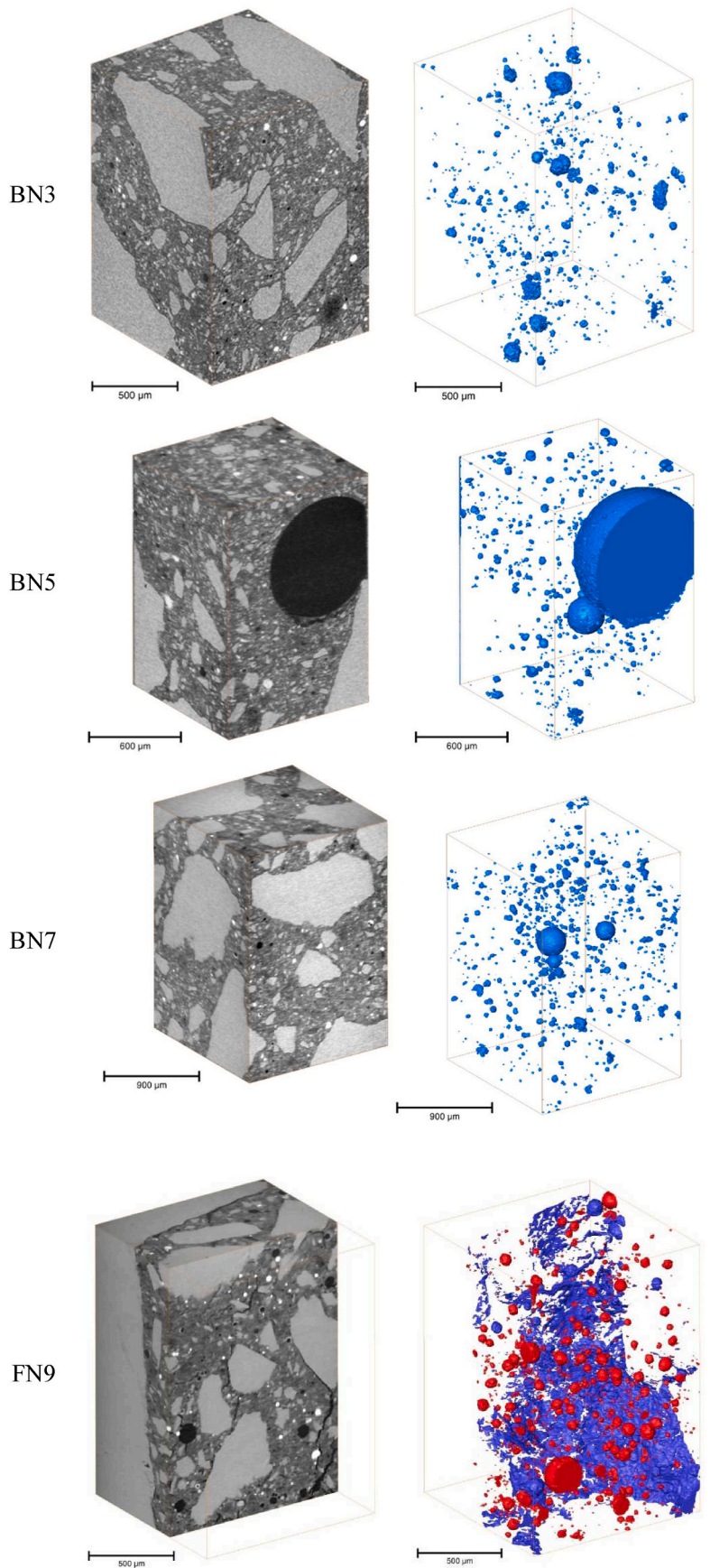
Data availability

Data will be made available on request.

Acknowledgments

Appendix A

Total scanned mortar volume	Model of Pores and cracks

SN3

SN5

SN7

BN3

BN5

BN7

FN9

. (*continued*).

References

[1] L. Bertolini, B. Elsener, P. Pedeferri, R. Polder, Corrosion of Steel in Concrete, 2004.

[2] K. Tuutti, Corrosion of Steel in Concrete, third ed., Uhlig's Corros. Handb, 1982, pp. 633–647, https://doi.org/10.1002/9780470872864.ch49.

[3] U.M. Angst, Challenges and opportunities in corrosion of steel in concrete, Mater. Struct. Constr. 51 (2018) 1–20, https://doi.org/10.1617/s11527-017-1131-6.

[4] U.M. Angst, Predicting the time to corrosion initiation in reinforced concrete structures exposed to chlorides, Cement Concr. Res. 115 (2019) 559–567, https://doi.org/10.1016/j.cemconres.2018.08.007.

[5] M.V.A. Florea, H.J.H. Brouwers, Chloride binding related to hydration products, Cement Concr. Res. 42 (2012) 282–290, https://doi.org/10.1016/j.cemconres.2011.09.016.

[6] Y. Guo, T. Zhang, W. Tian, J. Wei, Q. Yu, Physically and chemically bound chlorides in hydrated cement pastes: a comparison study of the effects of silica fume and metakaolin, J. Mater. Sci. 54 (2019) 2152–2169, https://doi.org/10.1007/s10853-018-2953-5.

[7] W. Wilson, F. Georget, K. Scrivener, Unravelling chloride transport/microstructure relationships for blended-cement pastes with the mini-migration method, Cement Concr. Res. 140 (2021), 106264, https://doi.org/10.1016/j.cemconres.2020.106264.

[8] C. Ouellet-Plamondon, G. Habert, Life Cycle Assessment (LCA) of Alkali-Activated Cements and Concretes, Woodhead Publishing Limited, 2014, https://doi.org/10.1533/9781782422884.5.663.

[9] D. Bondar, M. Basheer, S. Nanukuttan, Suitability of alkali activated slag/fly ash (AA-GGBS/FA) concretes for chloride environments: characterisation based on mix design and compliance testing, Construct. Build. Mater. 216 (2019) 612–621, https://doi.org/10.1016/j.conbuildmat.2019.05.043.

[10] D. Bondar, Q. Ma, M. Soutsos, M. Basheer, J.L. Provis, S. Nanukuttan, Alkali activated slag concretes designed for a desired slump, strength and chloride diffusivity, Construct. Build. Mater. 190 (2018) 191–199, https://doi.org/10.1016/j.conbuildmat.2018.09.124.

[11] M. Babaee, A. Castel, Chloride diffusivity, chloride threshold, and corrosion initiation in reinforced alkali-activated mortars: role of calcium, alkali, and silicate content, Cement Concr. Res. 111 (2018) 56–71, https://doi.org/10.1016/j.cemconres.2018.06.009.

[12] A. Runci, M. Serdar, J. Provis, Chloride-induced Corrosion of Steel Embedded in Alkali-Activated Materials: State of the Art, Simp. DOKTORSKOG Stud. GRAĐEVINARSTVA, Građevinski Fak. Zagreb, 2019, pp. 1–8, 9.-10. Rujna 2019.

[13] A. Blyth, C.A. Eiben, G.W. Scherer, C.E. White, Impact of activator chemistry on permeability of alkali-activated slags, J. Am. Ceram. Soc. 100 (2017) 4848–4859, https://doi.org/10.1111/jace.14996.

[14] J.L. Provis, R.J. Myers, C.E. White, V. Rose, J.S.J. Van Deventer, X-ray microtomography shows pore structure and tortuosity in alkali-activated binders, Cem, Concr. Res. 42 (2012) 855–864, https://doi.org/10.1016/j.cemconres.2012.03.004.

[15] H. Ye, L. Huang, Z. Chen, Influence of activator composition on the chloride binding capacity of alkali-activated slag, Cem. Concr. Compos. 104 (2019), 103368, https://doi.org/10.1016/j.cemconcomp.2019.103368.

[16] X. Ke, S.A. Bernal, J.L. Provis, Uptake of chloride and carbonate by Mg-Al and Ca-Al layered double hydroxides in simulated pore solutions of alkali-activated slag cement, Cement Concr. Res. 100 (2017) 1–13, https://doi.org/10.1016/j.cemconres.2017.05.015.

[17] J. Zhang, C. Shi, Z. Zhang, Chloride binding of alkali-activated slag/fly ash cements, Construct. Build. Mater. 226 (2019) 21–31, https://doi.org/10.1016/j.conbuildmat.2019.07.281.

[18] O. Kayali, M.S.H. Khan, M. Sharfuddin Ahmed, The role of hydrotalcite in chloride binding and corrosion protection in concretes with ground granulated blast furnace slag, Cem. Concr. Compos. 34 (2012) 936–945, https://doi.org/10.1016/j.cemconcomp.2012.04.009.

[19] M.S.H. Khan, O. Kayali, U. Troitzsch, Chloride binding capacity of hydrotalcite and the competition with carbonates in ground granulated blast furnace slag concrete, Mater. Struct. Constr. 49 (2016) 4609–4619, https://doi.org/10.1617/s11527-016-0810-z.

[20] Y. Ma, G. Wang, G. Ye, J. Hu, A comparative study on the pore structure of alkali-activated fly ash evaluated by mercury intrusion porosimetry, N2 adsorption and image analysis, J. Mater. Sci. 53 (2018) 5958–5972, https://doi.org/10.1007/s10853-017-1965-x.

[21] A. Noushini, A. Castel, J. Aldred, A. Rawal, Chloride diffusion resistance and chloride binding capacity of fly ash-based geopolymer concrete, Cem. Concr. Compos. (2019), 103290, https://doi.org/10.1016/j.cemconcomp.2019.04.006.

[22] P. Chindaprasirt, W. Chalee, Effect of sodium hydroxide concentration on chloride penetration and steel corrosion of fly ash-based geopolymer concrete under marine site, Construct. Build. Mater. 63 (2014) 303–310, https://doi.org/10.1016/j.conbuildmat.2014.04.010.

[23] N.K. Lee, H.K. Lee, Influence of the slag content on the chloride and sulfuric acid resistances of alkali-activated fly ash/slag paste, Cem. Concr. Compos. 72 (2016) 168–179, https://doi.org/10.1016/j.cemconcomp.2016.06.004.

[24] I. Ismail, S.A. Bernal, J.L. Provis, S. Hamdan, J.S.J. Van Deventer, Drying-induced changes in the structure of alkali-activated pastes, J. Mater. Sci. 48 (2013) 3566–3577, https://doi.org/10.1007/s10853-013-7152-9.

[25] J. Osio-Norgaard, J.P. Gevaudan, W.V. Srubar, A review of chloride transport in alkali-activated cement paste, mortar, and concrete, Construct. Build. Mater. 186 (2018) 191–206, https://doi.org/10.1016/j.conbuildmat.2018.07.119.

[26] M. Ben Haha, B. Lothenbach, G. Le Saout, F. Winnefeld, Influence of slag chemistry on the hydration of alkali-activated blast-furnace slag - Part I: effect of MgO,

[27] Cement Concr. Res. 41 (2011) 955–963, https://doi.org/10.1016/j.cemconres.2011.05.002.

M. Ben Haha, B. Lothenbach, G. Le Saout, F. Winnefeld, Influence of slag chemistry on the hydration of alkali-activated blast-furnace slag - Part II: effect of Al2O3, Cement Concr. Res. 42 (2012) 74–83, https://doi.org/10.1016/j.cemconres.2011.08.005.

[28] X. Ke, S.A. Bernal, O.H. Hussein, J.L. Provis, Chloride binding and mobility in sodium carbonate-activated slag pastes and mortars, Mater. Struct. Constr. 50 (2017) 1–13, https://doi.org/10.1617/s11527-017-1121-8.

[29] T. Yang, Z. Zhang, F. Zhang, Y. Gao, Q. Wu, Chloride and heavy metal binding capacities of hydrotalcite-like phases formed in greener one-part sodium carbonate-activated slag cements, J. Clean. Prod. 253 (2020), 120047, https://doi.org/10.1016/j.jclepro.2020.120047.

[30] R.R. Lloyd, J.L. Provis, J.S.J. Van Deventer, Microscopy and microanalysis of inorganic polymer cements. 1: remnant fly ash particles, Cement Concr. Res. 40 (2010) 1386–1392, https://doi.org/10.1016/j.cemconres.2010.04.008.

[31] X. Li, R. Snellings, M. Antoni, N.M. Alderete, M. Ben Haha, S. Bishnoi, Ö. Cizer, M. Cyr, K. De Weerdt, Y. Dhandapani, J. Duchesne, J. Haufe, D. Hooton, M. Juenger, S. Kamali-Bernard, S. Kramar, M. Marroccoli, A.M. Joseph, A. Parashar, C. Patapy, J.L. Provis, S. Sabio, M. Santhanam, L. Steger, T. Sui, A. Telesca, A. Vollpracht, F. Vargas, B. Walkley, F. Winnefeld, G. Ye, M. Zajac, S. Zhang, K.L. Scrivener, Reactivity tests for supplementary cementitious materials: RILEM TC 267-TRM phase 1, Mater. Struct. Constr. 51 (2018), https://doi.org/10.1617/s11527-018-1269-x.

[32] K. Scrivener, R. Snellings, B. Lothenbach, A Practical Guide to Microstructural Analysis of Cementitious Materials, 2015, https://doi.org/10.1201/b19074.

[33] V. Räsänen, V. Penttala, The pH measurement of concrete and smoothing mortar using a concrete powder suspension, Cement Concr. Res. 34 (2004) 813–820, https://doi.org/10.1016/j.cemconres.2003.09.017.

[34] J.L. Provis, K. Arbi, S.A. Bernal, D. Bondar, A. Buchwald, A. Castel, S. Chithiraputhiran, M. Cyr, A. Dehghan, K. Dombrowski-Daube, A. Dubey, V. Ducman, G.J.G. Gluth, S. Nanukuttan, K. Peterson, F. Puertas, A. van Riessen, M. Torres-Carrasco, G. Ye, Y. Zuo, RILEM TC 247-DTA round robin test: mix design and reproducibility of compressive strength of alkali-activated concretes, Mater. Struct. 52 (2019) 1–13, https://doi.org/10.1617/s11527-019-1396-z.

[35] (by flow table), EN 1015-3 Methods of Test for Mortar for Masonry — Part 3: Determination of Consistence of Fresh Mortar, 2004.

[36] EN 1015-7 Methods of Test for Mortar for Masonry - Part 7 Determination of Air Content of Fresh Mortar, 2004.

[37] EN 196-1 Methods of Testing Cement - Part 1: Determination of Strength, 2015.

[38] NT BUILD 492 Concrete, Mortar and Cement-Based Repair Materials: Chloride Micration Coefficent from Non-steady-state Migration Experiments.

[39] NT BUILD 443 Concrete, Hardened: Accelerated Chloride Penetration.

[40] Q. Yuan, C. Shi, F. He, G. De Schutter, K. Audenaert, K. Zheng, Effect of hydroxyl ions on chloride penetration depth measurement using the colorimetric method, Cement Concr. Res. 38 (2008) 1177–1180, https://doi.org/10.1016/j.cemconres.2008.04.003.

[41] Bs En 14629, Products and systems for the protection and repair of concrete structures - test methods - determination of chloride content in hardened concrete, Br. Stand. 3 (2007).

[42] ASTM C 1218 Standard Test Method for Water-Soluble Chloride in Mortar and Concrete, 2015.

[43] A.A. Sagues, E.I. Moreno, C. Andrade, Evolution of pH during in-situ leaching in small concrete cavities, Cement Concr. Res. 27 (1997) 1747–1759.

[44] Operator manual AutoPore IV (2017) 107–115.

[45] A.H. Ellison, R.B. Klemm, A.M. Schwartz, L.S. Grubb, D.A. Petrash, Contact angles of mercury on various surfaces and the effect of temperature, J. Chem. Eng. Data 12 (1967) 607–609, https://doi.org/10.1021/je60035a037.

[46] Z. Yu, G. Ye, The pore structure of cement paste blended with fly ash, Construct. Build. Mater. 45 (2013) 30–35, https://doi.org/10.1016/j.conbuildmat.2013.04.012.

[47] Y. Ma, J. Hu, G. Ye, The pore structure and permeability of alkali activated fly ash, Fuel 104 (2013) 771–780, https://doi.org/10.1016/j.fuel.2012.05.034.

[48] N. Alderete, Y. Villagrán, A. Mignon, D. Snoeck, N. De Belie, Pore structure description of mortars containing ground granulated blast-furnace slag by mercury intrusion porosimetry and dynamic vapour sorption, Construct. Build. Mater. 145 (2017) 157–165, https://doi.org/10.1016/j.conbuildmat.2017.03.245.

[49] V. Cnudde, A. Cwirzen, B. Masschaele, P.J.S. Jacobs, Porosity and microstructure characterization of building stones and concretes, Eng. Geol. 103 (2009) 76–83, https://doi.org/10.1016/j.enggeo.2008.06.014.

[50] L. Vincent, L. Vincent, P. Soille, Watersheds in digital spaces: an efficient algorithm based on immersion simulations, IEEE Trans. Pattern Anal. Mach. Intell. 13 (1991) 583–598, https://doi.org/10.1109/34.87344.

[51] C. Coletti, G. Cultrone, L. Maritan, C. Mazzoli, Combined multi-analytical approach for study of pore system in bricks: how much porosity is there? Mater. Char. 121 (2016) 82–92, https://doi.org/10.1016/j.matchar.2016.09.024.

[52] N.K. Lee, H.K. Lee, Setting and mechanical properties of alkali-activated fly ash/slag concrete manufactured at room temperature, Construct. Build. Mater. 47 (2013) 1201–1209, https://doi.org/10.1016/j.conbuildmat.2013.05.107.

[53] F. Puertas, S. Martínez-Ramírez, S. Alonso, T. Vázquez, Alkali-activated fly ash/slag cements. Strength behaviour and hydration products, Cement Concr. Res. 30 (2000) 1625–1632, https://doi.org/10.1016/S0008-8846(00)00298-2.

[54] I. Ismail, S.A. Bernal, J.L. Provis, R. San Nicolas, D.G. Brice, A.R. Kilcullen, S. Hamdan, J.S.J. Van Deventer, Influence of fly ash on the water and chloride permeability of alkali-activated slag mortars and concretes, Construct. Build.

Mater. 48 (2013) 1187–1201, https://doi.org/10.1016/j. conbuildmat.2013.07.106.

[55] X. Yao, T. Yang, Z. Zhang, Compressive strength development and shrinkage of alkali-activated fly ash–slag blends associated with efflorescence, Mater. Struct. Constr. 49 (2016) 2907–2918, https://doi.org/10.1617/s11527-015-0694-3.

[56] A. Runci, M. Serdar, Chloride-Induced corrosion of steel in alkali-activated mortars based on di ff erent precursors, Materials 13 (2020) 5244, https://doi.org/ 10.3390/ma13225244, 1–17.

[57] G.J.G. Gluth, K. Arbi, S.A. Bernal, D. Bondar, K.D. Ashish, D. Vilma, D. Karl, P. Pipilikaki, S.L.A. Valcke, G. Ye, Y. Zuo, J.L. Provis, RILEM TC 247-DTA round robin test : carbonation and chloride penetration testing of alkali-activated concretes, Mater. Struct. 3 (2020), https://doi.org/10.1617/s11527-020-1449-3.

[58] A. Noushini, A. Castel, The effect of heat-curing on transport properties of low-calcium fly ash-based geopolymer concrete, Construct. Build. Mater. 112 (2016) 464–477, https://doi.org/10.1016/j.conbuildmat.2016.02.210.

[59] R.R. Lloyd, J.L. Provis, J.S.J. Van Deventer, Pore solution composition and alkali diffusion in inorganic polymer cement, Cement Concr. Res. 40 (2010) 1386–1392, https://doi.org/10.1016/j.cemconres.2010.04.008.

[60] S.A. Bernal, J.L. Provis, D.G. Brice, A. Kilcullen, P. Duxson, J.S.J. Van Deventer, Accelerated carbonation testing of alkali-activated binders significantly underestimates service life: the role of pore solution chemistry, Cement Concr. Res. 42 (2012) 1317–1326, https://doi.org/10.1016/j.cemconres.2012.07.002.

[61] C. Andrade, Design and evaluation of service life through concrete electrical resistivity, Rev. ALCONPAT. 8 (2018) 264–279, https://doi.org/10.21041/ra. v8i3.349.

[62] R. Kumar, B. Bhattacharjee, Porosity, pore size distribution and in situ strength of concrete, Cement Concr. Res. 33 (2003) 155–164, https://doi.org/10.1016/S0008-8846(02)00942-0.

[63] C. Monticelli, M.E. Natali, A. Balbo, C. Chiavari, F. Zanotto, S. Manzi, M. C. Bignozzi, A study on the corrosion of reinforcing bars in alkali-activated fly ash mortars under wet and dry exposures to chloride solutions, Cement Concr. Res. 87 (2016) 53–63, https://doi.org/10.1016/j.cemconres.2016.05.010.

[64] S. Diamond, Mercury porosimetry. An inappropriate method for the measurement of pore size distributions in cement-based materials, Cement Concr. Res. 30 (2000) 1517–1525, https://doi.org/10.1016/S0008-8846(00)00370-7.

[65] Y. Jun, S. Yoon, J.E. Oh, A comparison study for chloride-binding capacity between alkali-activated fly ash and slag in the use of seawater, Appl. Sci. 7 (2017), https://doi.org/10.3390/app7100971.

[66] P.S. Mangat, O.O. Ojedokun, Influence of curing on pore properties and strength of alkali activated mortars, Construct. Build. Mater. 188 (2018) 337–348, https://doi. org/10.1016/j.conbuildmat.2018.07.180.

[67] G. Fang, W.K. Ho, W. Tu, M. Zhang, Workability and mechanical properties of alkali-activated fly ash-slag concrete cured at ambient temperature, Construct. Build. Mater. 172 (2018) 476–487, https://doi.org/10.1016/j. conbuildmat.2018.04.008.

[68] S. Narimani Zamanabadi, S.A. Zareei, P. Shoaei, F. Ameri, Ambient-cured alkali-activated slag paste incorporating micro-silica as repair material: effects of alkali activator solution on physical and mechanical properties, Construct. Build. Mater. 229 (2019), 116911, https://doi.org/10.1016/j.conbuildmat.2019.116911.

[69] Q. Ma, S.V. Nanukuttan, P.A.M. Basheer, Y. Bai, C. Yang, Chloride transport and the resulting corrosion of steel bars in alkali activated slag concretes, Mater. Struct. Constr. 49 (2016) 3663–3677, https://doi.org/10.1617/s11527-015-0747-7.

[70] X. Hu, C. Shi, D. Zhu, G. de Schutter, Investigation on influential factors on chloride concentration index of cement-based materials by pore solution expression method, Construct. Build. Mater. 231 (2020), 117135, https://doi.org/10.1016/j. conbuildmat.2019.117135.

[71] X. Hu, C. Shi, Z. Shi, L. Zhang, Compressive strength, pore structure and chloride transport properties of alkali-activated slag/fly ash mortars, Cem. Concr. Compos. 104 (2019), 103392, https://doi.org/10.1016/j.cemconcomp.2019.103392.

[72] R.J. Myers, S.A. Bernal, J.L. Provis, A thermodynamic model for C-(N-)A-S-H gel: CNASH-ss. Derivation and validation, Cem, Concr. Res. 66 (2014) 27–47, https:// doi.org/10.1016/j.cemconres.2014.07.005.

[73] M.R. Karim, M.M. Hossain, M.F.M. Zain, M. Jamil, F.C. Lai, Durability properties of a non-cement binder made up of pozzolans with sodium hydroxide, Construct. Build. Mater. 138 (2017) 174–184, https://doi.org/10.1016/j. conbuildmat.2017.01.130.

[74] I. Garcia-Lodeiro, A. Fernandez-Jimenez, A. Palomo, Hydration kinetics in hybrid binders: early reaction stages, Cem. Concr. Compos. 39 (2013) 82–92, https://doi. org/10.1016/j.cemconcomp.2013.03.025.

[75] J. Zhang, Y. Ma, J. Zheng, J. Hu, J. Fu, Z. Zhang, H. Wang, Chloride diffusion in alkali-activated fly ash/slag concretes : role of slag content , water/binder ratio , alkali content and sand-aggregate ratio Chloride diffusion in alkali-activated fly ash/slag concretes : role of slag content , water/binder, Construct. Build. Mater. 261 (2020), 119940, https://doi.org/10.1016/j.conbuildmat.2020.119940.

[76] H.N. Yoon, S.M. Park, H.K. Lee, Effect of MgO on chloride penetration resistance of alkali-activated binder, Construct. Build. Mater. 178 (2018) 584–592, https://doi. org/10.1016/j.conbuildmat.2018.05.156.

[77] S. Sui, F. Georget, H. Maraghechi, W. Sun, K. Scrivener, Towards a generic approach to durability: factors affecting chloride transport in binary and ternary cementitious materials, Cement Concr. Res. 124 (2019), 105783, https://doi.org/ 10.1016/j.cemconres.2019.105783.